



Structural topology optimization with simultaneous stress and displacement constraints considering multiple load cases

Felix Rutsch¹ · Marc Fina² · Steffen Freitag²

Received: 11 March 2024 / Revised: 10 December 2024 / Accepted: 13 December 2024 / Published online: 4 March 2025
© The Author(s) 2025

Abstract

In this paper, a structural topology optimization approach is presented considering stress and displacement constraints using different load cases. This is motivated by structural engineering applications. A short review on different types of constraints is presented, distinguishing respective measures on a global and local basis. It is identified that local stress and displacement constraints represent common engineering problems most closely and allow for a wide variety of applications, especially different displacement limits for different structural regions. In order to solve the proposed multiconstrained formulation, stress-constrained optimization with the Augmented Lagrangian method is extended to include displacement constraints simultaneously. The implementation of multiple load cases is discussed. This leads to a highly modular approach that can easily be adapted to different engineering problems. The corresponding gradient is derived and the optimization is performed using a steepest descent method. The effectiveness of this approach is proven based on the example of an L-shaped structure and a two-span beam.

Keywords Topology optimization · Augmented Lagrangian method · Displacement constraints · Stress constraints · Volume minimization

1 Introduction

Topology optimization (TO) is highly promising in structural engineering, as it enables the design of more efficient structures and reduces resource consumption. However, when applying TO to typical structural engineering problems, some difficulties are faced. Real-world structures are subjected to a multitude of different loading situations. Limits to stresses and displacements have to be considered for different load cases and different points within the structure. Classical off-the-shelf implementations of structural TO cannot cover all these applications. Instead, it is proposed

to customize the optimization problem itself in order to replicate the engineering problem as closely as possible. In this paper, several pieces are put together to form a multi-constrained problem. Corresponding solution techniques are discussed and it is investigated how the individual aspects interact with each other.

The first published approach to TO is the so-called compliance minimization introduced by Bendsøe and Kikuchi (1988). It uses a strain energy based measure of performance as objective while implementing a volume constraint. This formulation has been extensively investigated and efficient solution techniques have been developed, see, e.g., Bendsøe and Sigmund (2003) for an overview.

In a typical structural engineering problem, requirements for the structural performance are given, to be fulfilled with minimum material usage. This leads to volume minimization problems, instead. Considering the structural performance, stress-constrained (Yang and Chen 1996; Duysinx and Bendsøe 1998) and displacement-constrained (Yin and Yang 2001; Huang and Xie 2009) volume minimization approaches are of particular interest. Furthermore, constraints need to be applied for multiple load cases, particularly including self-weight. This requires some additional

Responsible editor: Julián Andrés Norato

✉ Marc Fina
marc.fina@kit.edu

¹ Cyber-Physical Simulation Group, Technical University of Darmstadt, Dolivostr. 15, 64293 Darmstadt, Hessen, Germany

² Institute for Structural Analysis, Karlsruhe Institute of Technology, Kaiserstr. 12, 76131 Karlsruhe, Baden-Württemberg, Germany

considerations, see Bruyneel and Duysinx (2004). Giraldo-Londoño and Paulino (2020) discuss the self-weight in the context of stress-based TO.

Another important aspect to be distinguished in TO problems is whether global or local performance measures are used. A global measure takes the form of a single value for the whole structure, such as the total strain energy. In contrast to that stress-based failure criteria have to be considered at all points within the structure. Likewise, displacements may be limited for specific degrees of freedom.

Such local constraints pose a serious challenge in TO, due to their large number of entries (Yang and Chen 1996). Many different implementations for stress constraints in particular are discussed in the literature, which can be subdivided into two basic strategies.

First, the local stress values can be aggregated into a single measure on a global basis by employing the maximum stress. To ensure the differentiability, a smooth approximation of the maximum is required, see, e.g., Duysinx and Sigmund (1998). As a further extension, regional stress measures can be taken into account as shown in Le et al. (2009) and París et al. (2010). Recent advances in this field are given in Norato et al. (2022).

Second, different approaches based on the penalty method can be used. In this case, additional terms representing the local constraints are added to the objective function. Of particular interest is the Augmented Lagrangian (AL) Method (Birgin and Martínez 2014). It is applied for stress-constrained TO with multiple load cases in Fancello and Pereira (2003). An implementation of this approach is also presented in Giraldo-Londoño and Paulino (2021). A comparison of local and global constraint approaches is presented in París et al. (2008) and da Silva et al. (2021).

In addition to stress constraints, stiffness requirements have to be satisfied simultaneously in engineering practice. Thus, it seems useful to consider a multiconstrained formulation including both constraints in a single TO problem. This is addressed in Bruggi and Duysinx (2012), where a volume minimization problem with stress and compliance (strain energy) constraints is expounded. In this case, a limit for the stress, as well as a maximum total strain energy have to be specified. However, typical stiffness requirements in engineering are rather specified as limits for nodal displacements. Further, a single global limit cannot cover all applications, such as different displacement limits in different parts of the structure. Therefore, it seems useful to implement local displacement constraints, directly.

A comprehensive literature research revealed that while stress and displacement limits are frequently used in TO of trusses, see, e.g., Ringertz (1985), few papers consider stresses and displacements simultaneously in the context of continuum structures. An early implementation can be found in Deqing et al. (2000). Ramani (2010) solves the stress- and

displacement-constrained volume minimization with a heuristic TO approach, while Wang et al. (2019) and Xia et al. (2020) use gradient-based TO with the SIMP approach and global constraints.

However, local constraints are used in none of these references. In particular, the AL method is successfully used for stress-constrained TO and shown to be more effective than global constraint approaches in the comparative study by da Silva et al. (2021). Therefore, it should be investigated whether this advancement for stress constraints can also be transferred to local displacement constraints in a combined approach.

In this paper, a multiconstrained volume minimization problem with local constraints in terms of stresses and displacements is solved using the AL method. Multiple load cases including gravity load, i.e., self-weight of the structure, are implemented in this context. The highlights of this paper can be summarized as follows:

- Extension of local stress-constrained structural TO based on the AL method to consider displacement constraints simultaneously.
- Discussion on the influence of the position of displacement-constrained nodes in the multiconstrained context.
- A comprehensive study on optimal penalty parameters for TO with local stress and displacement constraints.

The paper is structured as follows. Section 2 starts by introducing fundamentals of TO. As a next step, different types of constraints are distinguished, in order to motivate and develop the proposed problem formulation.

Section 3 addresses the numerical solution of the optimization problem by applying the AL method and deriving the corresponding gradient.

Numerical examples are presented in Sect. 4. For comparison with other references, the L-shaped benchmark example is shown (Sect. 4.1). Illustrating the application of the proposed formulation for structural engineering problems, a two-span beam is discussed (Sect. 4.2). Concluding remarks can be found in Sect. 5.

2 Problem formulation

2.1 Governing equations

Let Ω denote a two-dimensional continuous domain, its boundary defined as $\Gamma = \Gamma_u \cup \Gamma_\sigma$. At the Dirichlet boundary Γ_u displacements are prescribed as $\bar{\mathbf{u}}$, whereas at the Neumann boundary Γ_σ tractions $\bar{\mathbf{t}}$ are given. Further, a body force \mathbf{b} , such as gravity load, may act in Ω . The equilibrium condition can be written in terms of the weak form

$$\int_{\Omega} \boldsymbol{\varepsilon}^T(\mathbf{v}) \mathbf{C} \boldsymbol{\varepsilon}(\mathbf{u}) \, d\Omega = \int_{\Gamma_{\sigma}} \mathbf{v}^T \bar{\mathbf{t}} \, d\Gamma_{\sigma} + \int_{\Omega} \mathbf{v}^T \mathbf{b} \, d\Omega, \quad (1a)$$

$$\mathbf{u} = \bar{\mathbf{u}}, \quad \mathbf{v} = \mathbf{0} \quad \text{at} \quad \Gamma_u, \quad (1b)$$

where \mathbf{u} represents the displacement vector and \mathbf{v} stands for an arbitrary test function. Using Voigt notation, strains are given by $\boldsymbol{\varepsilon} = [u_{1,1}, u_{2,2}, u_{2,1} + u_{1,2}]$, assuming small deformations. In case of linear elasticity, stresses are computed as $\boldsymbol{\sigma} = \mathbf{C} \boldsymbol{\varepsilon}$. For isotropic materials, the material matrix \mathbf{C} can be expressed in terms of two independent variables, such as Young's modulus E and Poisson's ratio ν .

To obtain a numerical solution of (1), the domain is discretized by means of the Finite Element (FE) Method. 4-node quadrilateral plane stress elements are used, forming a regular mesh of square-shaped elements with side length l_e . For a base material with Young's modulus E_0 , the corresponding base element stiffness matrix \mathbf{k}_0 is

$$\mathbf{k}_0 = \int_{\Omega_e} \mathbf{B}^T \mathbf{C}_0 \mathbf{B} \, d\Omega_e, \quad (2)$$

where \mathbf{B} is the strain-displacement transformation matrix and \mathbf{C}_0 is computed using E_0 . Both these matrices are constant, because a regular mesh is used, i.e., every element has the same geometry.

Likewise, an element load vector \mathbf{f}_0 is defined, taking into account the self-weight of an element. In case of a 4-node regular quadrilateral element, assuming the load to be equally distributed on the nodes $n = 1, \dots, 4$, it can be expressed as

$$\mathbf{f}_0 = [(\mathbf{f}_0)_1, \dots, (\mathbf{f}_0)_4] \quad (\mathbf{f}_0)_n = \frac{V_e}{4} \gamma_0 \mathbf{g}, \quad (3)$$

where γ_0 denotes the effective mass density of the base material (gravity load/volume) and \mathbf{g} is a unit vector indicating the direction of gravity. V_e is the (constant) element volume, computed in the two-dimensional case as $V_e = A_e t$, where A_e is the element area and t denotes the element thickness.

The topology of the structure is described by the physical relative density function $\bar{\rho}(\mathbf{x})$ and $\mathbf{x} \in \Omega$. Values of $0 < \bar{\rho}_{\min} \leq \bar{\rho} \leq 1$ are considered, where the base material has a density of one. Through filtering and projection as described in Sect. 2.3, the physical density is closely related to the design density ρ , which is used as design variable for the optimization. Implementing a value $\bar{\rho}_e$ for each finite element, the corresponding element stiffness matrix $\mathbf{k}_e(\bar{\rho}_e)$ can be computed by scaling \mathbf{k}_0 with the Young's modulus E_e depending on $\bar{\rho}_e$, as follows:

$$\mathbf{k}_e(\bar{\rho}_e) = \frac{E_e(\bar{\rho}_e)}{E_0} \mathbf{k}_0. \quad (4)$$

Using a continuous range of density values enables the implementation of efficient gradient-based minimization algorithms. Nonetheless, the generated topologies should feature either base material or no material. To suppress intermediate densities, the Solid Isotropic Material with Penalization (SIMP) approach is used, see, e.g., Bendsøe (1989) and Zhou and Rozvany (1991). The relation of the element Young's modulus and the physical density is defined as

$$E_e^{\text{SIMP}}(\bar{\rho}_e) = \bar{\rho}_e^p E_0, \quad (5)$$

introducing the SIMP penalization parameter p . When computing the element stiffness matrix (4) with this approach, a minimum physical density $\bar{\rho}_{\min}$ has to be implemented in order to avoid singularity due to zero stiffness elements. Further, a relation between self-weight and physical density has to be specified. The relative mass density can be interpolated linearly such that the element load vector is written as

$$\mathbf{f}_e(\bar{\rho}_e) = \frac{\gamma_e(\bar{\rho}_e)}{\gamma_0} \mathbf{f}_0 = \bar{\rho}_e \mathbf{f}_0. \quad (6)$$

However, the parasitic effect described by Bruyneel and Duysinx (2004) has to be taken into account at this point. Combining the SIMP approach (5) with the linear self-weight interpolation (6) involves the issue that the ratio between self-weight and stiffness becomes infinite as $\bar{\rho}_e$ approaches zero. This leads to problems in regions that should be generated as void, as some material remains there to support the self-weight. Therefore, at least one of the intermediate density interpolation approaches for the stiffness and the self-weight has to be adjusted. Bruyneel and Duysinx (2004) modified the SIMP approach with a linear section for low density values, while using the self-weight interpolation according to (6). In Zhang et al. (2020), a non-linear self-weight interpolation is used by additionally applying the SIMP approach also for the self-weight. In the present paper, the approach proposed by Giraldo-Londoño and Paulino (2020) is implemented: for those TO problems where the self-weight is considered, the SIMP approach (5) is replaced by the RAMP (Rational Approximations of Material Properties) approach originally introduced by Stolpe and Svanberg (2001), as

$$E_e^{\text{RAMP}}(\bar{\rho}_e) = \frac{\bar{\rho}_e}{1 + \hat{p}(1 - \bar{\rho}_e)} E_0, \quad (7)$$

where \hat{p} denotes the RAMP penalization parameter. Further, an initial density of $\bar{\rho}_0 = 0.5$ instead of 1 is useful in this context.

Assembling all \mathbf{k}_e and \mathbf{f}_e yields the global stiffness matrix \mathbf{K} and load vector \mathbf{F} , respectively. Exterior loads other than gravity are added to \mathbf{F} . The global displacement

vector \mathbf{U} can be obtained as solution to the well-known system of linear equations

$$\mathbf{K}\mathbf{U} = \mathbf{F}, \tag{8}$$

where the Dirichlet boundary conditions (1b) have to be considered.

Afterward, stresses in the base material can be computed as

$$(\sigma_0)_e = \mathbf{B} \mathbf{C}_0 \mathbf{u}_e. \tag{9}$$

Here, the index e indicates that there is only one stress evaluation point for each element, located at the element's center.

To reduce the stress components in Voigt notation σ to a scalar-valued equivalent stress σ_{eq} , a widely used measure is the von Mises stress. It can be computed by means of an operator matrix \mathbf{M} according to Duysinx and Bendsøe (1998), defined as

$$(\sigma_{eq,0})_e = \sqrt{(\sigma_0)_e^T \mathbf{M} (\sigma_0)_e} \quad \mathbf{M} = \begin{bmatrix} 1 & -\frac{1}{2} & 0 \\ -\frac{1}{2} & 1 & 0 \\ 0 & 0 & 3 \end{bmatrix}. \tag{10}$$

For elements with intermediate material density, stresses are computed according to the ε -relaxed approach introduced by Cheng and Guo (1997). It is implemented to avoid the singularity phenomenon, see, e.g., Duysinx and Bendsøe (1998) and Le et al. (2009), which is a major challenge in stress-based TO. A stress interpolation function $f_\sigma(\bar{\rho}_e)$ is defined as

$$f_\sigma(\bar{\rho}_e) = \frac{\bar{\rho}_e}{\varepsilon(1 - \bar{\rho}_e) + \bar{\rho}_e}, \tag{11}$$

such that

$$(\sigma_{eq})_e = f_\sigma(\bar{\rho}_e) (\sigma_{eq,0})_e, \tag{12}$$

where $(\sigma_{eq,0})_e$ is computed for the base material stress vector obtained from (9). Depending on the point of view, this approach can be seen as modifying the Young's modulus, interpolating the stress or relaxing the stress constraint. For the parameter ε in (11), a continuation approach can be implemented such that $\varepsilon \rightarrow 0$ during the iterative optimization, see, e.g., Cheng and Guo (1997). In the present paper, a constant value of $\varepsilon = 0.2$ is used, as discussed by da Silva et al. (2019). An overview of the interpolation functions for different density-related properties is shown in Fig. 1, where the corresponding parameters are specified in Table 1.

2.2 Optimization problem

A multitude of different formulations of a TO problem can be found in the literature of the past years. Summing up a basic underlying principle, these formulations can be subdivided into two categories:

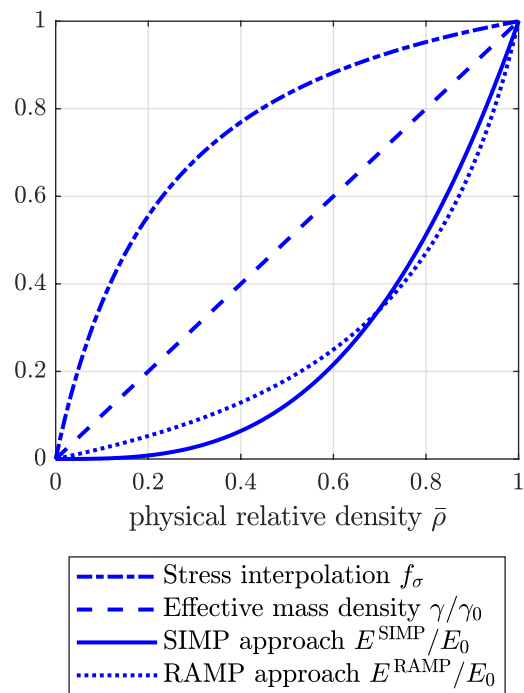


Fig. 1 Interpolation of different properties for intermediate densities using the parameters given in Table 1

Table 1 Interpolation parameters

Parameter	Value	Publication	
SIMP penalization	p	3	Amstutz (2010)
RAMP penalization	\hat{p}	3.5	Giraldo-Londoño and Paulino (2020)
Stress interpolation	ε	0.2	da Silva et al. (2019)

- (a) *Performance maximization* uses some kind of structural performance as objective function, while a fixed volume/amount of material is specified as constraint.
- (b) *Volume minimization* seeks to minimize the amount of material used for the structure, while structural performance requirements are defined as constraints. This can be viewed as reverse approach compared to (a).

For a given engineering problem, it has to be investigated, which optimization problem represents it in the best way. In many practical applications, the volume of the structure is undefined beforehand, but specific requirements for the performance are given. For example, stresses may be limited and maximum allowable displacements defined for specific domains. Solving a problem of this type with a performance maximization approach, e.g., compliance minimization, requires to define a volume constraint in advance. In essence, a suitable volume has to be estimated that leads to an optimized structure satisfying the

requirements. Using a more systematic approach, the volume can be varied as part of an outer optimization loop, calculating several optimized structures in an iterative manner, see, e.g., Freitag et al. (2022).

However, using a volume minimization problem directly incorporating the technical constraints, only a single TO run is necessary. Therefore, the presented approach focuses entirely on volume minimization, as it most closely represents problems commonly found in engineering practice.

The volume minimization problem in a general form is given by

$$\min_{\rho_{\min} \leq \rho_e \leq 1} V_f = \frac{1}{V_{\max}} \sum_{e=1}^{N_e} \bar{\rho}_e V_e, \quad (13a)$$

$$\text{s.t. } g_k = \frac{P_k}{(P_{\text{lim}})_k} - 1 \leq 0 \quad \forall \mathbf{x}_k \in \underline{\Omega}, \quad (13b)$$

$$\mathbf{K}\mathbf{U} = \mathbf{F}, \quad (13c)$$

where the objective function (13a) is formulated in terms of a volume fraction V_f . It is computed as a sum of all element volumes weighted with the respective element density $\bar{\rho}_e$, divided by the maximum volume V_{\max} .

For the constraint $g_k(\bar{\rho})$ (13b), a general structural performance P and a corresponding requirement P_{lim} are used. The requirement is fulfilled if the utilization level, defined as the quotient of both, is lower or equal to one. Depending on the type of performance measure, such constraints can take two different forms:

- Global constraints* are based on a performance measure for the entire structure, thus P is a single scalar value.
- Local constraints* are based on a point-wise performance measure, in the form of a vector with components P_k . The design is acceptable if $g_k \leq 0$ for each point \mathbf{x}_k of the considered set $\underline{\Omega} \subseteq \Omega$, see (13b).

Furthermore, in some publications (e.g., Wang et al. 2019; Xia et al. 2020) constraints are formulated using the difference of performance and its limit, such as

$$P - P_{\text{lim}} \leq 0. \quad (14)$$

This is generally equivalent to the quotient-based formulation (13b) for $P_{\text{lim}} > 0$, but the corresponding constraint term differs by a factor of P_{lim} , affecting the AL method, see Sect. 3.1. However, the constraint (14) should not be applied if $P_{\text{lim}} < 0$, for example, due to a limit for displacements in negative direction. In contrast to that an utilization level P/P_{lim} can deal with negative values for P and P_{lim} . Further, the utilization level provides a more descriptive measure to

assess the fulfillment of the constraint in the author's opinion. Therefore, the formulation P/P_{lim} is preferred in this work.

To complement the preceding general discussion, the performance requirements considered in the context of this publication are explicitly specified:

Stress: In order to avoid structural damage, stresses should be limited. Depending on the application, different stress measures are useful for the assessment. A widely used measure is the von Mises stress, see (10). Therefore, a stress constraint can specify that the admissible von Mises stress may not be exceeded at any point. As stresses are evaluated at one point per element according to (9), it is convenient to also impose the constraint on a per-element basis. Thus, the stress constraint is formulated as

$$\frac{(\sigma_{\text{eq}})_e}{\sigma_{\text{lim}}} - 1 \leq 0 \quad \forall e = 1, \dots, N_e. \quad (15)$$

Volume minimization problems with this type of constraint have been investigated extensively, see, e.g., Yang and Chen (1996), Duysinx and Bendsøe (1998), and da Silva and Cardoso (2017). Further, multiple materials can be used at the same time by specifying different limits $(\sigma_{\text{lim}})_e$ for different elements e , see Ramani (2010). Aggregating the element stress constraints into a single global measure, the maximum of all element stresses can be considered (Duysinx and Sigmund 1998).

Displacement: In many applications, the displacement of the structure under load has to be limited. To include this in the optimization problem, a straightforward approach is to implement constraints based on nodal displacements (Yin and Yang 2001). A corresponding formulation is

$$\frac{(u_i)_n}{(u_{i,\text{lim}})_n} - 1 \leq 0 \quad \forall n = 1, \dots, N_n, \quad (16)$$

where $(u_{i,\text{lim}})_n$ denotes the limit for the i th component of the displacement vector \mathbf{u} , at node n of the FE mesh. Thus, different limits can be specified for different (sets of) points n , depending on the circumstances of the given problem. This possibility is lost when using a single global displacement constraint, i.e., the maximum nodal displacement (Chen et al. 2020).

Strain energy: Other stiffness-based TO formulations use the strain energy as performance measure, commonly referred to as compliance. On a global level, it is defined as

$$C = \mathbf{U}^T \mathbf{K} \mathbf{U} = \mathbf{U}^T \mathbf{F}, \quad (17)$$

which is the objective of the well-known compliance minimization approach introduced by Bendsøe and Kikuchi

(1988). Adhering to volume minimization problems discussed in the presented work, strain energy/compliance can be used as constraint (Bruggi and Duysinx 2012), such as

$$\frac{C}{C_{lim}} \leq 1, \tag{18}$$

where a global limit C_{lim} has to be specified. Recalling the weak form (1), it can be seen that C provides the work of the external loads and is equal to the internal strain energy of the structure. A connection to the displacements \mathbf{U} is highlighted by (17): C can be interpreted as (multiple of the) average displacement of the loaded domains, justifying the name compliance. However, regarding points other than those of load application, a conversion from C to specific nodal displacements is ambiguous. Further, computing the strain energy on a per-element basis, local strain energy constraints are also used in the literature, see, e.g., Ramani (2010). As shown by Li et al. (1999), such an approach is equivalent to considering element-wise stresses. Because the global strain energy (17) is typically computed as a sum of all element-wise strain energies, it can be viewed as a multiple of the average strain energy.

To decide on a specific formulation, it is proposed to use the following TO problem:

$$\min_{\rho_{min} \leq \rho_e \leq 1} V_f = \frac{1}{V_{max}} \sum_{e=1}^{Ne} \bar{\rho}_e V_e, \tag{19a}$$

$$\text{s.t. } \frac{(\sigma_{eq})_e^j}{\sigma_{lim}} - 1 \leq 0 \quad \forall e, j, \tag{19b}$$

$$\frac{(u_i)_n^j}{(u_{i,lim})_n} - 1 \leq 0 \quad \forall n, i, j, \tag{19c}$$

$$\mathbf{K}(\bar{\rho}) \mathbf{U}^j(\bar{\rho}) = \mathbf{F}^j(\bar{\rho}) \quad \forall j. \tag{19d}$$

It includes stress and displacement constraints, as they are the most common requirements in engineering practice. Local constraints are used to allow for a wide variety. Theoretically, a distinct limit can be specified for every single component. Of particular interest are different displacement limits $(u_{i,lim})_n$ for different sets of points. Further, different load cases \mathbf{F}^j are considered, including the gravity load $\mathbf{F}(\bar{\rho})$. The objective is to identify a unified topology that satisfies all specified requirements. Therefore, a multiconstrained formulation is used, incorporating all mentioned constraints simultaneously as shown in Fig. 2.

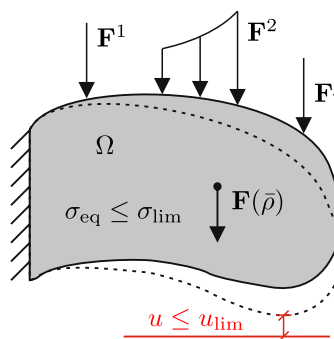


Fig. 2 Design domain, boundary conditions, and constraints of the TO problem

2.3 Filtering and projection

2.3.1 Density filter

To ensure mesh independence and avoid the checkerboarding phenomenon, see, e.g., Jog and Haber (1996), density filtering is implemented. Based on the design density ρ , a filtered density $\bar{\rho}$ is computed as given in Bourdin (2001)

$$\bar{\rho}_i = \frac{\sum_{j \in \vartheta_i} w(\mathbf{x}_j) V_j \rho_j}{\sum_{j \in \vartheta_i} w(\mathbf{x}_j) V_j}, \tag{20}$$

where \mathbf{x}_j denotes the coordinates of the element center of element j . ϑ_i is the filter domain of element i , consisting of all elements j whose center is within radius R of the center of element i . The weighting function $w(\mathbf{x}_j)$ is defined as

$$w(\mathbf{x}_j) = R - |\mathbf{x}_j - \mathbf{x}_i|. \tag{21}$$

2.3.2 Threshold projection

To reduce the amount of intermediate density, a threshold projection scheme is used, see Xu et al. (2009). The physical density $\bar{\rho}$ is computed according to Wang et al. (2010), as

$$\bar{\rho}_e = \frac{\tanh(\beta\kappa) + \tanh(\beta(\bar{\rho}_e - \kappa))}{\tanh(\beta\kappa) + \tanh(\beta(1 - \kappa))}, \tag{22}$$

where $\kappa \in (0, 1)$ controls the position of the inflection point. The parameter $\beta > 0$ determines the sharpness of the projection, where for larger β less intermediate density is present in the topology.

It is pointed out that the threshold projection changes the minimum density, $\rho_{min} = \bar{\rho}_{min} \neq \bar{\rho}_{min}$. In particular, β is increased throughout the optimization iterations, see Sect. 3.3. This means, if a constant minimum design density ρ_{min} is used, minimum physical density $\bar{\rho}_{min}$ will not be constant during

the optimization procedure. Potential numerical issues, e.g., ill-conditioning of $\mathbf{K}(\bar{\rho})$, are related to the physical density. Therefore, it is proposed to specify a constant $\bar{\rho}_{\min}$, instead. The corresponding limit ρ_{\min} can be obtained using the inverse of (22), as

$$\rho_{\min} = \kappa + \frac{1}{\beta} \operatorname{atanh} \left(-\tanh(\beta\kappa) + \bar{\rho}_{\min} \left(\tanh(\beta\kappa) \tanh(\beta(1-\kappa)) \right) \right). \tag{23}$$

The minimum design density ρ_{\min} according to (23) is computed initially and every time β is changed, i.e., for every subproblem update.

3 Solution strategies

3.1 AL Method

The AL method is implemented in order to solve the constrained optimization problem (19) using techniques of unconstrained optimization. The stress-constrained formulation by da Silva and Cardoso (2017) is extended to include local displacement constraints and multiple load cases j , including gravity load in particular. The AL function corresponding to the optimization problem (19) is given by

$$L = V_f(\bar{\rho}) \tag{24a}$$

$$+ \sum_{j=1}^{N_{lc}} \left(\frac{r_\sigma}{2} \sum_{e=1}^{N_\sigma} \left(\max \left(0, \frac{(\lambda_\sigma)_e^j}{r_\sigma} + (g_\sigma)_e^j \right) \right)^2 \tag{24b}$$

$$+ \frac{r_u}{2} \sum_{d=1}^{N_u} \left(\max \left(0, \frac{(\lambda_u)_d^j}{r_u} + (g_u)_d^j \right) \right)^2 \tag{24c}$$

$$+ (\Lambda^j)^T (\mathbf{K}(\bar{\rho}) \mathbf{U}^j(\bar{\rho}) - \mathbf{F}^j(\bar{\rho})). \tag{24d}$$

The objective function is extended with terms representing the stress and displacement constraints

$$(g_\sigma)_e = \frac{(\sigma_{eq})_e}{\sigma_{lim}} - 1, \tag{25}$$

$$(g_u)_d = \frac{u_d}{(u_{lim})_d} - 1, \tag{26}$$

corresponding to (19b) and (19c), respectively. The index d counts the displacement degrees of freedom u_d as part of the global displacement vector \mathbf{U} . As discussed in Fancello and

Pereira (2003), constraint terms of different load cases are simply added together. Further, the equilibrium condition (19d) is included for every load case j and multiplied with an arbitrary adjoint vector Λ^j .

For every constraint term g , a corresponding Lagrange multiplier λ is introduced. Likewise, a distinct penalty parameter r can be used for every single constraint. In this paper, only a single stress- and a single displacement-related penalty parameter r_σ and r_u are distinguished.

3.2 Gradient

To solve the proposed optimization problem with a gradient-based algorithm, the derivative of the AL function (24) w.r.t. the design variables ρ is required. First, the objective function is formulated in terms of physical densities $\bar{\rho}$, related to ρ by filtering and projection. Thus, the chain rule is applied, see, e.g., Sigmund (2007):

$$\frac{dL(\bar{\rho})}{d\rho} = \frac{dL(\bar{\rho})}{d\bar{\rho}} \frac{d\bar{\rho}}{d\rho} \tag{27}$$

where the derivative of the threshold projection (22) can be computed element wise as

$$\frac{d\bar{\rho}_k}{d\rho_k} = \frac{\beta (\operatorname{sech}(\beta(\bar{\rho}_k - \kappa)))^2}{\tanh(\beta\kappa) + \tanh(\beta(1-\kappa))}. \tag{28}$$

Complementary, for the derivative of the filtering scheme (20) one has to incorporate the influence of neighboring elements in the respective filter domain ϑ_k . Therefore, the derivatives have to be summed as follows:

$$\frac{d\bar{\rho}}{d\rho_k} = \sum_{e \in \vartheta_k} \frac{d\bar{\rho}_e}{d\rho_k}, \tag{29}$$

where the individual derivative terms are given as

$$\frac{d\bar{\rho}_e}{d\rho_k} = \frac{w(\mathbf{x}_k)V_k}{\sum_{i \in \vartheta_e} w(\mathbf{x}_i)V_i}. \tag{30}$$

As a next step, the derivative of the AL function (24) w.r.t $\bar{\rho}_k$ is computed separately for each summand

$$\frac{\partial L}{\partial \bar{\rho}_k} = \frac{\partial V_f}{\partial \bar{\rho}_k} + \sum_{j=1}^{N_{lc}} \left(\frac{\partial \mathcal{S}^j}{\partial \bar{\rho}_k} + \frac{\partial \mathcal{D}^j}{\partial \bar{\rho}_k} + \frac{\partial \mathcal{Q}^j}{\partial \bar{\rho}_k} \right), \tag{31}$$

where \mathcal{S}^j , \mathcal{D}^j , and \mathcal{Q}^j are introduced to abbreviate the j -th stress, displacement, and equilibrium terms of (24b) to (24d), respectively.

Computing the first term of (31), the derivative of the volume fraction V_f is

$$\frac{\partial V_f}{\partial \bar{\rho}_k} = \frac{V_k}{\sum_{e=1}^{N_e} V_e} = \frac{V_k}{V_{\max}}. \tag{32}$$

Regarding the second term of (31), the derivative of the stress term S^j (24b) is computed in accordance with da Silva and Cardoso (2017), as

$$\frac{\partial S^j}{\partial \bar{\rho}_k} = \sum_{e=1}^{N_\sigma} (h_\sigma)_e^j \frac{\partial (\sigma_{\text{eq}})_e^j}{\partial \bar{\rho}_k}, \tag{33}$$

where $(h_\sigma)_e^j$ is defined as

$$(h_\sigma)_e^j = \frac{1}{\sigma_{\text{lim}}} \max(0, (\lambda_\sigma)_e^j + r_\sigma (g_\sigma)_e^j). \tag{34}$$

Recalling the stress computation (9), (10), (12), the corresponding derivative is given by

$$\frac{\partial (\sigma_{\text{eq}})_e^j}{\partial \bar{\rho}_k} = \frac{\partial f_\sigma(\bar{\rho}_e)}{\partial \bar{\rho}_k} (\sigma_{\text{eq},0})_e^j + \frac{f_\sigma(\bar{\rho}_e)}{(\sigma_{\text{eq},0})_e^j} (\mathbf{a}_e^j)^T \frac{\partial (\mathbf{u}_e^j)^T}{\partial \bar{\rho}_k}, \tag{35}$$

introducing the auxiliary variable $(\mathbf{a}_e^j)^T$ as

$$(\mathbf{a}_e^j)^T = (\mathbf{u}_e^j)^T \mathbf{B}_e^T \mathbf{C}_0 \mathbf{M} \mathbf{C}_0 \mathbf{B}_e. \tag{36}$$

The derivative of the stress interpolation function f_σ (11) is given by

$$\frac{\partial f_\sigma(\bar{\rho}_k)}{\partial \bar{\rho}_k} = \frac{\varepsilon}{(\varepsilon(1 - \bar{\rho}_k) + \bar{\rho}_k)^2}, \tag{37}$$

which is nonzero for $k = e$ only. Based on this property, summation for all elements e needs to be performed only for the second summand of (35) when substituting (35), (36), and (37) into (33). As a result, the derivative of the stress term is obtained as

$$\begin{aligned} \frac{\partial S^j}{\partial \bar{\rho}_k} &= \underbrace{(h_\sigma)_k^j \frac{\partial f_\sigma(\bar{\rho}_k)}{\partial \bar{\rho}_k} (\sigma_{\text{eq},0})_k^j}_{s_k^j} \\ &+ \underbrace{\sum_{e=1}^{N_\sigma} (h_\sigma)_e^j \frac{f_\sigma(\bar{\rho}_e)}{(\sigma_{\text{eq},0})_e^j} (\mathbf{a}_e^j)^T \mathbf{H}_e \frac{\partial \mathbf{U}^j}{\partial \bar{\rho}_k}}_{S^j}, \end{aligned} \tag{38}$$

where the localization operator \mathbf{H}_e relates the element displacement vector \mathbf{u}_e to the global vector \mathbf{U} as $\mathbf{u}_e = \mathbf{H}_e \mathbf{U}$.

Concerning the third term of (31), the derivative of the displacement term D^j (24c) is given by

$$\frac{\partial D^j}{\partial \bar{\rho}_k} = \sum_{d=1}^{N_u} (h_u)_d^j \frac{\partial u_d^j}{\partial \bar{\rho}_k} = \sum_{d=1}^{N_u} \underbrace{(h_u)_d^j \mathbf{e}_d}_{\mathbf{D}^j} \frac{\partial \mathbf{U}^j}{\partial \bar{\rho}_k}, \tag{39}$$

where

$$(h_u)_d^j = \frac{1}{(u_{\text{lim}})_d} \max(0, (\lambda_u)_d^j + r_u (g_u)_d^j) \tag{40}$$

and $\mathbf{e}_d = [0, 0, \dots, 1, \dots, 0]$ is the unit vector corresponding to the degree of freedom d such that $u_d = \mathbf{e}_d \mathbf{U}$.

Finally, the fourth term of (31), i.e., the derivative of the equilibrium term Q^j (24d) is computed as

$$\begin{aligned} \frac{\partial Q^j}{\partial \bar{\rho}_k} &= (\boldsymbol{\Lambda}^j)^T \left(\frac{\partial \mathbf{K}}{\partial \bar{\rho}_k} \mathbf{U}^j + \mathbf{K} \frac{\partial \mathbf{U}^j}{\partial \bar{\rho}_k} - \frac{\partial \mathbf{F}^j}{\partial \bar{\rho}_k} \right) \\ &= (\boldsymbol{\Lambda}^j_k)^T \underbrace{\left(\frac{\partial \mathbf{k}_k}{\partial \bar{\rho}_k} \mathbf{u}_k^j - \frac{\partial \mathbf{f}_k^j}{\partial \bar{\rho}_k} \right)}_{q_k^j} + \underbrace{(\boldsymbol{\Lambda}^j)^T \mathbf{K}}_{\mathbf{Q}^j} \frac{\partial \mathbf{U}^j}{\partial \bar{\rho}_k}. \end{aligned} \tag{41}$$

For the derivatives of \mathbf{K} and \mathbf{F} w.r.t $\bar{\rho}_k$, only the contribution of element k has to be taken into account. Deriving the element stiffness matrix (4), which is computed either with the SIMP approach (5) or the RAMP approach (7), yields

$$\frac{\partial \mathbf{k}_k^{\text{SIMP}}(\bar{\rho}_k)}{\partial \bar{\rho}_k} = p \bar{\rho}_k^{p-1} \mathbf{k}_0, \tag{42}$$

$$\frac{\partial \mathbf{k}_k^{\text{RAMP}}(\bar{\rho}_k)}{\partial \bar{\rho}_k} = \frac{\hat{p} + 1}{(\hat{p} \bar{\rho}_k - \hat{p} - 1)^2} \mathbf{k}_0, \tag{43}$$

while the derivative of the element load vector (6) is given by

$$\frac{\partial \mathbf{f}_k^j(\bar{\rho}_k)}{\partial \bar{\rho}_k} = \mathbf{f}_0^j, \tag{44}$$

where loads other than gravity load are independent of ρ .

By aggregating the derivatives related to stress, displacement and equilibrium from Eqs. (38), (39) and (41), it follows

$$\frac{\partial L}{\partial \bar{\rho}_k} = \frac{\partial V_f}{\partial \bar{\rho}_k} + \sum_{j=1}^{N_{\text{lc}}} \left(s_k^j + q_k^j + (\mathbf{S}^j + \mathbf{D}^j + \mathbf{Q}^j) \frac{\partial \mathbf{U}^j}{\partial \bar{\rho}_k} \right). \tag{45}$$

In order to avoid computing the derivative of \mathbf{U}^j , the corresponding prefactors are set to zero. This can be achieved by choosing the arbitrary adjoint vectors $\boldsymbol{\Lambda}^j$ accordingly, yielding a system of linear equations for each load case

$$\mathbf{K} \boldsymbol{\Lambda}^j = -\mathbf{S}^j - \mathbf{D}^j, \tag{46}$$

such that the derivative of the AL function is

$$\frac{\partial L}{\partial \rho_k} = \frac{V_k}{V_{\max}} + \sum_{j=1}^{N_{ic}} s_k^j + q_k^j. \quad (47)$$

In combination with the chain rule (27), Eqs. (46) and (47) provide a modular system to compute the gradient of the objective function featuring multiple load cases and constraints. If certain constraints are not applied in a specific load case, the terms \mathbf{S} and s or \mathbf{D} are simply omitted. Likewise, gravity load can be deactivated by ignoring the corresponding terms. For every load case, two systems of linear equations have to be solved, one for the FE analysis (8) and one for the adjoint vector (46). Using stress and displacement constraints simultaneously requires the same number of these systems to be solved compared to using just one type of constraint, because both types are handled using the same adjoint vector. Further, the computational effort is not much higher for multiple load cases than for a single load case (Fancello and Pereira 2003). This is due to the fact that the stiffness matrix \mathbf{K} is constant and therefore has to be triangularized only once, such that more load cases just require more back-substitution operations.

3.3 Minimization algorithm

With the AL method, the optimization problem is decomposed into a series of minimization subproblems with constant Lagrange multipliers. The update scheme for a general Lagrange multiplier λ_i with regard to the a -th subproblem writes as

$$\lambda_i^{(a+1)} = \max(0, \lambda_i^{(a)} + r_i^{(a)} g_i(\bar{\rho})), \quad (48)$$

where $\lambda = \mathbf{0}$ is set initially. Based on the sensitivity analysis presented in Sect. 3.2, the minimization problem is solved by a gradient-based algorithm. A numerical solution is obtained in an iterative manner, using N_{it}^{sub} iterations per subproblem. N_{it}^{min} specifies the number of iterations to reach the last subproblem, while N_{it}^{tot} is the total number of iterations.

Since a detailed investigation of different minimization algorithms is not the focus of this work, an elementary approach using a Steepest Descent Method (SDM) is implemented as an example. Concerning other minimization algorithms, reference is made to Svanberg (1987) for the Method of Moving Asymptotes (MMA), which is widely adopted in TO. The fundamental update scheme for the b -th iteration step of the SDM is

$$\rho_e^{(b+1)} = \rho_e^{(b)} - \Psi \nabla_{\rho} L^{(b)}, \quad (49)$$

where Ψ denotes the step length. Here, the algorithm presented in da Silva et al. (2021) is implemented. The full algorithm is provided in Appendix A.1.

During the optimization, the parameters β and r_i are increased from β_0 to β_{\max} and $\frac{r_{i,0}}{N_i}$ to $\frac{r_{i,\max}}{N_i}$, respectively. The penalty parameters are normalized by the corresponding number of constraints N_i , i.e., divided by N_{σ} for the stress and N_u for the displacement penalty parameter. For the full update scheme based on da Silva et al. (2021) see Appendix A.2.

4 Numerical examples

In this section, numerical examples are discussed in order to investigate the effectiveness of the proposed method. The algorithm is implemented using MATLAB (Mathworks 2023), based on the framework provided by Andreassen et al. (2011). Several numerical parameters have to be specified. Table 2 presents an overview of the default values used for all subsequent examples, unless stated otherwise.

4.1 L-Shaped structure

The first example is a structure with an L-shaped design domain shown in Fig. 3. This structure is frequently used as a benchmark example especially for stress-based TO formulations, see, e.g., Duysinx and Bendsøe (1998). An Overview of different L-shaped structures is presented in Le et al. (2009). In this section, the presented multiconstrained TO approach is tested for the L-shaped structure and compared with TO using only a single type of constraints. Further, the influence of the stress and displacement penalty parameters to the results is investigated.

The design domain is discretized using a FE mesh consisting of $N_e = 25,600$ elements with a side length of $l_e = 0.005$ m, based on a 200×200 grid. A single point load F is applied at the tip, distributed over a length of 0.05 m to avoid a stress singularity. To enable a comparison with other references, no self-weight is considered in

Table 2 Numerical parameters used throughout the following examples

Parameter	Symbol	Value
Minimum physical density	$\bar{\rho}_{\min}$	1e−9
Iteration steps per subproblem	N_{it}^{sub}	20
Initial projection sharpness	β_0	0.1
Maximum projection sharpness	β_{\max}	5
Inflection point of projection	κ	0.5
Initial penalty parameters	$r_{i,0}$	0.01
Maximum penalty parameters	$r_{i,\max}$	1e4
Iterations to last subproblem	N_{it}^{min}	1000
Iterations in total	N_{it}^{tot}	1200

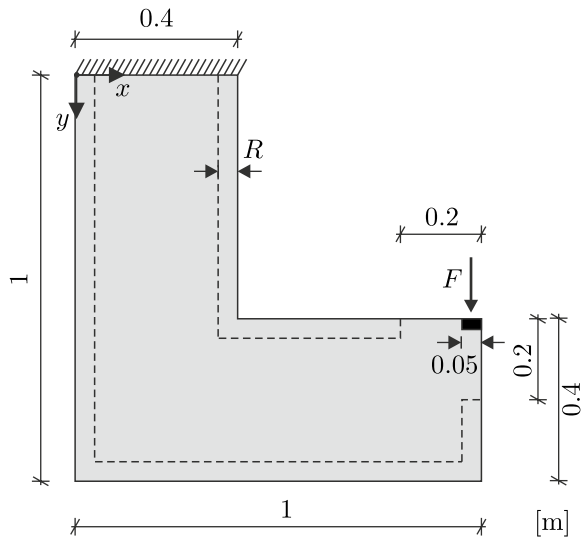


Fig. 3 Design domain and boundary conditions for the L-shaped structure

this example and the SIMP approach (5) is used. Along the edges, a padding region of width equal to the filter radius R is implemented, as indicated by the dashed lines in Fig. 3. It serves the purpose of avoiding boundary effects due to filtering, see, e.g., Clausen and Andreassen (2017). In addition to Table 2, the values of the parameters used for this example in particular are given in Table 3. To facilitate a direct comparison, identical boundary conditions and parameter values are used, as presented in da Silva et al. (2021). However, a fixed number of iterations instead of a stop criterion is applied for the last subproblem. Further, a larger Young’s Modulus $E_0 = 10^5 \text{ N/m}^2$ is implemented in order to achieve small deformations regarding the additional displacement constraints. The choice of E_0 does not affect the solution if only the stress constraints are considered.

Table 3 Parameters used for the L-shaped structure

Parameter	Symbol	Value	Unit
Young’s modulus	E_0	1 e5	N/m^2
Poisson’s ratio	ν	0.3	–
plate thickness	t	1	m
load	F	1	N
limit stress	σ_{lim}	70	N/m^2
vertical disp limit	$u_{y,\text{lim}}$	0.003	m
initial (uniform) phys. density	$\bar{\rho}_0$	1	–
filter radius	R	0.015	m

4.1.1 Stress-constrained

For reference, the optimization is performed using only stress constraints, applied for all elements except those in the padding region. The fulfillment of the constraints is assessed based on the quotient $\sigma_{\text{eq},e}/\sigma_{\text{lim}}$ for each element, where the global stress utilization level η_σ is defined as

$$\eta_\sigma = \max_e \left(\frac{\sigma_{\text{eq},e}}{\sigma_{\text{lim}}} \right), \tag{50}$$

using the maximum equivalent stress of all elements for which the stress constraint is applied.

The resulting optimized topology and the corresponding stresses and displacements are shown in Fig. 4a. It can be seen that a bend at the inner corner of the design domain is generated in order to avoid a stress concentration at this point.

By testing the reduced algorithm using only the stress constraints, it is verified that the results are similar to the ones presented for the corresponding algorithm in da Silva et al. (2021). Volume fraction and stress utilization are compared in Table 4. Note that a different filtering strategy and filter radius is implemented in da Silva et al. (2021).

4.1.2 Displacement-constrained

The results of a purely displacement-constrained optimization are investigated next. A vertical limit $u_{y,\text{lim}}$ is implemented for all nodes in the design domain. In general, the fulfillment of the displacement constraints is assessed by calculating the utilization level

$$\eta_u^{(i)} = \max_{d \in (i)} \left(\frac{u_d}{u_{\text{lim}}^{(i)}} \right) \tag{51}$$

for all structural regions i . The results of the purely displacement-constrained TO are shown in Fig. 4b. It can be seen that the optimized structure does comply with the displacement limit. Concerning the stresses, a stress concentration at the inner corner is observed, exceeding the 70 N/m^2 used as limit for the stress-constrained TO in Fig. 4a. It is mentioned that for many varieties of structural regions with displacement constraints, e.g., using only the bottom row of nodes, a purely displacement-constrained formulation does not lead to a useful solution. This aspect is discussed in detail in

Table 4 Comparison with a reference example

Method	V_f	η_σ
Proposed method, stress constr. only	0.206	1.005
AL + SDM in da Silva et al. (2021)	0.237	1.002

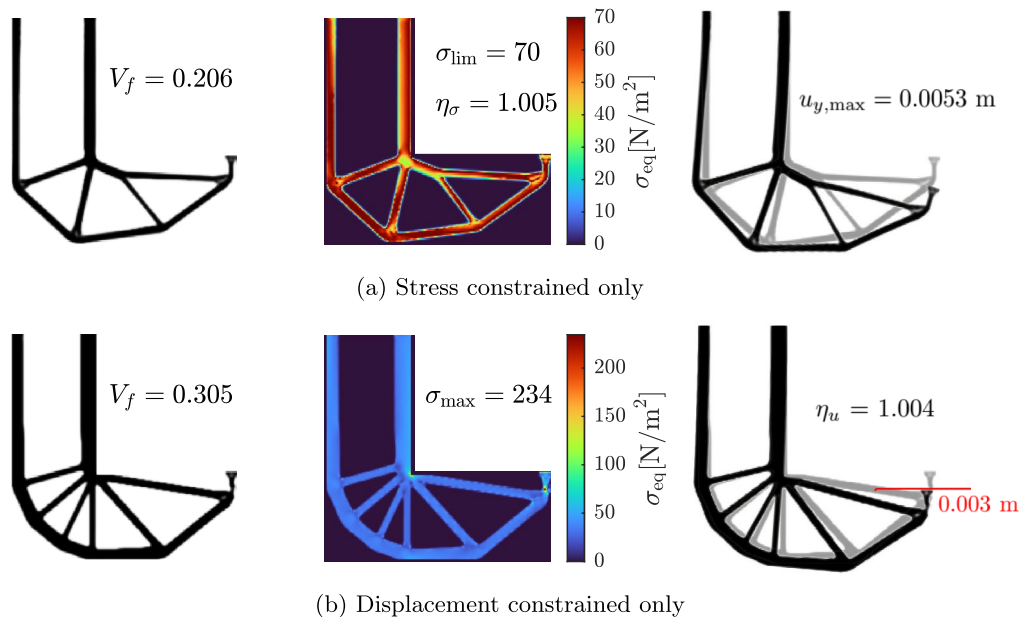


Fig. 4 L-shaped structure—Optimal topology (left), von Mises stresses (middle), and deformed structure with a scaling factor 25 (right) for **(a)** stress-constrained only and **(b)** displacement-constrained only

Sect. 4.1.4. Future research might investigate dynamic displacement constraints, which are only active in high density regions such that the constraint is only applied to elements that are actually part of the final structure. However, this is out of the scope of this work.

4.1.3 Stress- and displacement-constrained

Subsequently, TO for the L-shaped structure using stress and displacement constraints simultaneously is discussed. Regarding the corresponding limit values, three different cases are distinguished as

- (i) $\sigma_{\text{lim}} = 70 \text{ N/m}^2$, $u_{y,\text{lim}} = 0.01 \text{ m}$,
- (ii) $\sigma_{\text{lim}} = 70 \text{ N/m}^2$, $u_{y,\text{lim}} = 0.003 \text{ m}$,
- (iii) $\sigma_{\text{lim}} = 500 \text{ N/m}^2$, $u_{y,\text{lim}} = 0.003 \text{ m}$,

where case (ii) denotes the default stress and displacement limits according to Table 3. For this case, the corresponding optimal topology is presented in Fig. 5b. First, it is noted that the structure does comply with the displacement limit. Concerning the stresses, it is observed that most of the elements do not reach the stress limit, but some are fully utilized, particularly at the inner corner. Such a total utilization level of one for both the stress and the displacement constraint is not achieved for the default limits by any of the formulations using only a single type of constraints, as shown in Fig. 4. It is also noted that the topology of Fig. 5b has a larger volume fraction than any of the topologies in Fig. 4.

Using a less restrictive displacement limit of $u_{y,\text{lim}} = 0.01 \text{ m}$, case (i), the topology of Fig. 5a is obtained. Here, it is observed that the structure is highly utilized in terms of stresses, but the displacement is lower than the specified limit. Therefore, it is concluded that the displacement constraint is not critical in this case. This is also highlighted by the fact that the topology of Fig. 5a has almost the same volume fraction V_f and a similar shape as the topology presented in Fig. 4a, which is obtained using a purely stress-constrained formulation.

Likewise, the use of a stronger material with $\sigma_{\text{lim}} = 500 \text{ N/m}^2$, case (iii), is examined. The corresponding topology is presented in Fig. 5c. A stress concentration at the inner corner is observed, but the limit stress is not reached. This means that the stress constraint is not critical in this case. The structure is similar to the purely displacement-constrained version of Fig. 4b and has almost the same volume fraction.

Comparing the inner corners of the topologies in Fig. 5, there is a homogeneous stress distribution for case (i), a slight stress concentration for case (ii), and a high peak stress is observed for case (iii).

Summarized, it is observed that for some cases, the multiconstrained approach leads to the same topologies as obtained by an approach using only a single type of constraints. However, if both the stress and the displacement constraint necessitate a similarly large volume fraction, the multiconstrained approach does generate a structure that has a total utilization level of one for both the stress and the

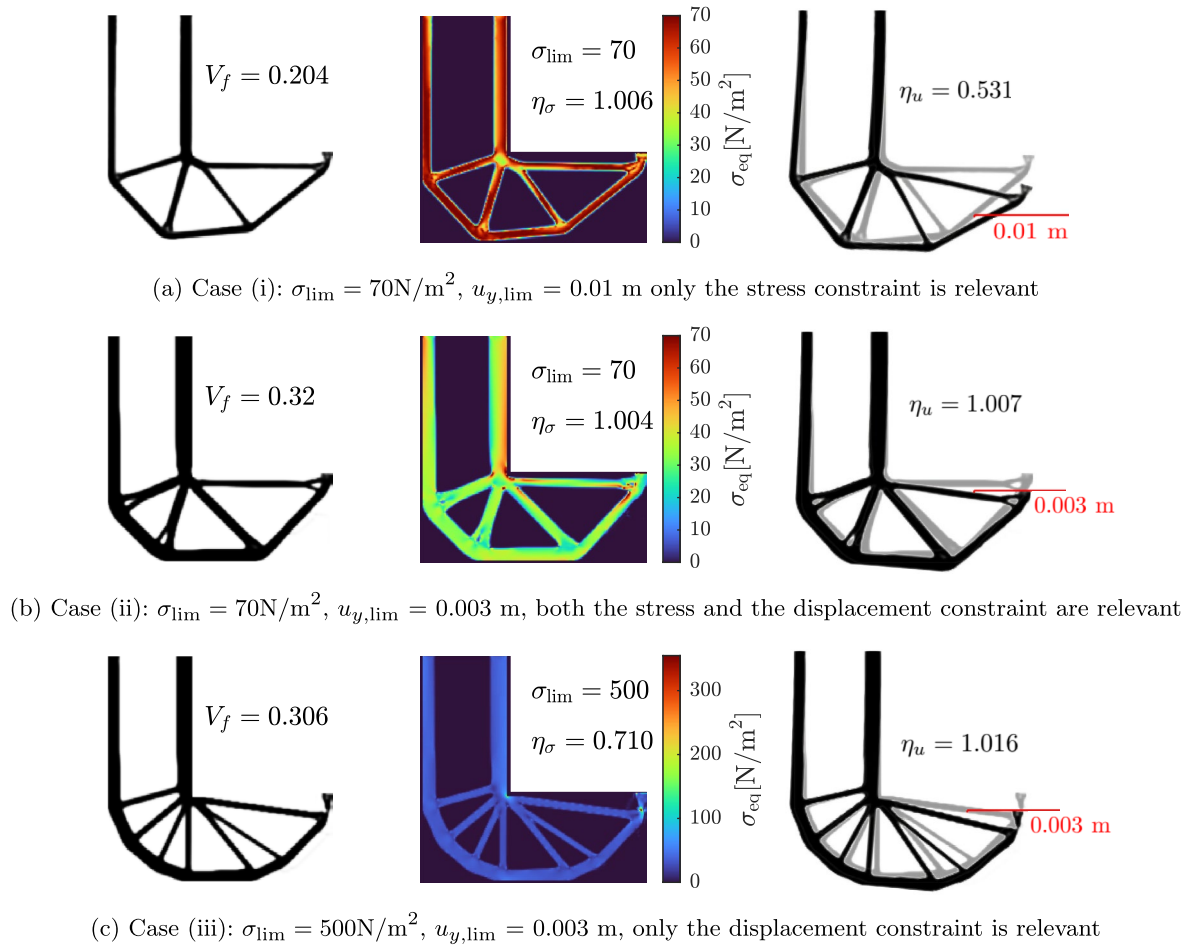


Fig. 5 L-shaped structure—Optimal topology (left), von Mises stresses (middle), and deformed structure with a scaling factor 25 (right), using stress and displacement constraints simultaneously

displacement constraint. This solution can only be generated using both constraints simultaneously. If one type of constraints is not critical, it can theoretically be ignored, but this is often unknown beforehand. Moreover, using

only displacement constraints may lead to elements with extremely high stresses which can be avoided by adding stress constraints.

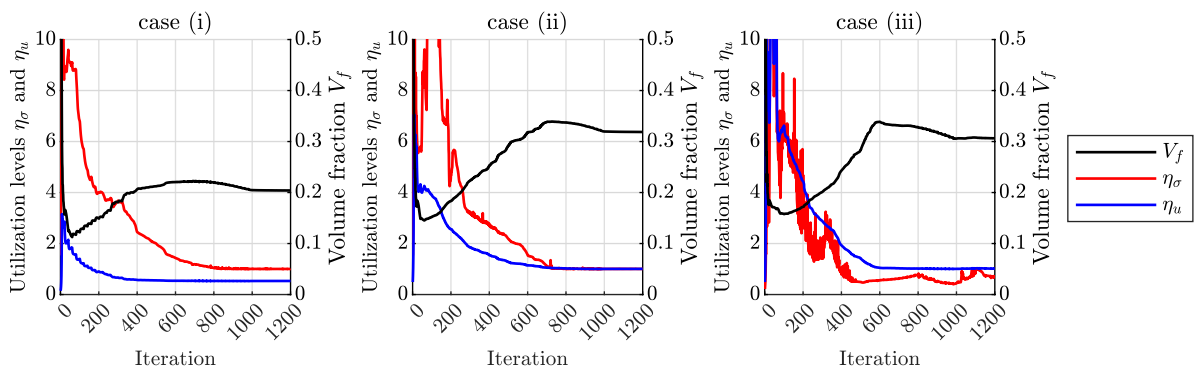


Fig. 6 Objective and constraints during the optimization of the L-shaped structure with different stress and displacement limits specified as cases (i) to (iii) in Sect. 4.1.3

4.1.4 Optimization history

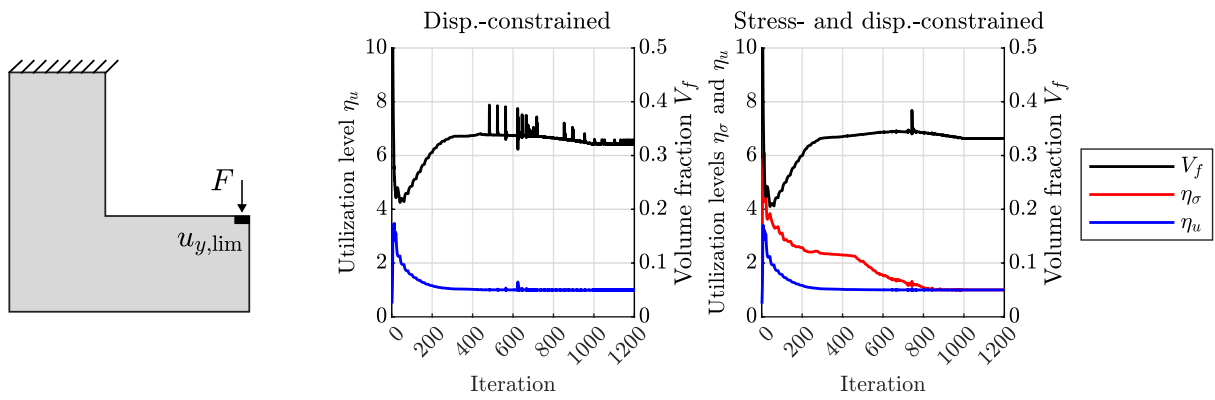
Figure 6 shows the history of the volume fraction (objective) and the stress and displacement utilization level (constraints) during the optimization of the topologies presented in Fig. 5, distinguishing the cases (i) to (iii) introduced in Sect. 4.1.3. The results are interpreted as follows: the objective converges with an increasing number of iterations, highlighting the success of the optimization. If a constraint is relevant to the problem, the corresponding utilization level converges to one. If not, a value smaller than one is reached.

While displacement constraints are applied to all nodes for the topologies presented in Fig. 5, some applications specify displacement limits for certain points only. Therefore, it is investigated what happens when the displacement constraint is applied to the nodes at the load application or to the nodes along the lower edge of the design domain, using the default stress and displacement limits of case (ii).

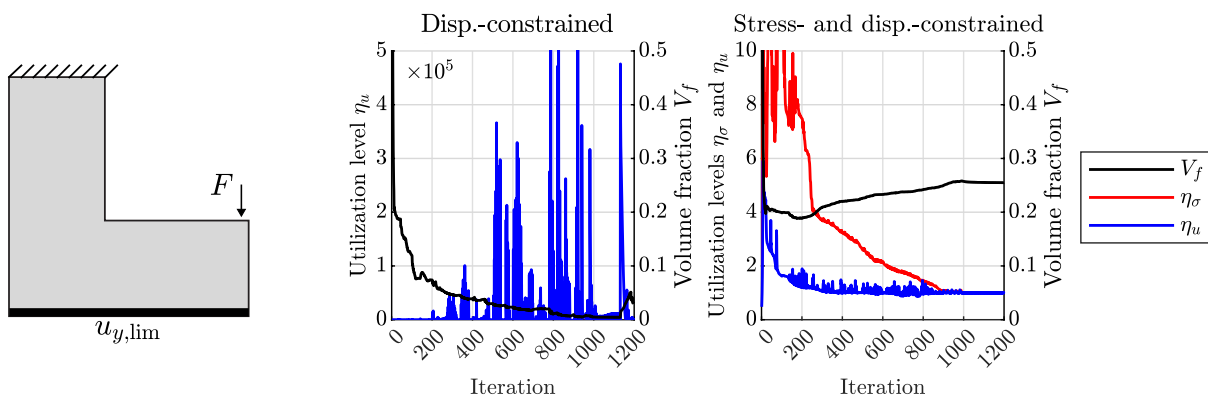
Constraining the load application nodes, it is observed that the results shown in Fig. 7a are similar to case (ii) in

Fig. 6. This is because applying the displacement constraint to only the load application nodes is closely related to applying it to every node, as the maximum displacement occurs at the load application points.

Constraining the bottom row of nodes, the optimization fails when using only the displacement constraints, but converges when using both constraints as shown in Fig. 7b. This is due to the fact that in the former case, there is no effective constraint for the elements located in the load application area. Consequently, these load-bearing elements are generated with low density to minimize volume, which leads to numerical problems. This issue is avoided in the latter case by adding the stress constraints. Summarized, TO using only displacement constraints will diverge for certain choices of the displacement-constrained set of nodes, but can be stabilized by adding stress constraints for all elements.



(a) Displacement constraint applied to the loaded nodes



(b) Displacement constraint applied to the bottom row of nodes

Fig. 7 Objective and constraints during the optimization of the L-shaped structure with different displacement-constrained sets of nodes, using the default limit values of case (ii)

4.1.5 Penalty parameters

The proper choice of stress and displacement penalty parameters is examined in the context of the proposed formulation. First, it is recalled that the penalty parameters are normalized by the number of constraints N_σ or N_u . This is particularly relevant for the displacements, where N_u varies a lot for different sets of nodes. The update scheme for the penalty parameters is given by (A8) in the appendix. For the initial stress penalty parameter $r_{\sigma}^{(a=0)} = \frac{r_{\sigma,0}}{N_\sigma}$, a value of $r_{\sigma,0} = 0.01$ is suggested in da Silva et al. (2021). Applying this for the displacements as well, $r_{\sigma,0} = r_{u,0} = 0.01$ is consistently used throughout this work. Regarding the maximum penalty parameters $r_{\sigma,max}$ and $r_{u,max}$, a study is performed using the L-shaped structure with parameter values according to Table 3. The volume fraction and corresponding utilization level of the resulting topology depending on the maximum penalty parameter are plotted for the displacement in Fig. 8a and for the stress in Fig. 8b, respectively. To investigate the interaction of stress and displacement penalty parameters, three curves are presented in Fig. 8a, b for different values of the other maximum penalty parameter.

First, it is observed that both utilization levels η_i converge to one for an increase of the corresponding maximum penalty parameter $r_{i,max}$. Considering the interaction, a higher value of $r_{u,max}$ generally leads to a lower η_σ and vice versa. The volume fraction increases for higher values $r_{i,max}$. Based on this study, it can be confirmed that the

selection of $r_{i,max} = 1e4$ for both the maximum stress and the maximum displacement penalty parameter given in Table 2 is a good choice to get reliable results. This is motivated due to the fact that the utilization levels η_i are converged to nearly one at this point. Higher values of $r_{i,max}$ result in very small improvements of η_i while reducing the efficiency due to higher V_f . Moreover, numerical problems can occur for very high $r_{i,max}$.

4.2 Two-span beam

The second example represents a two-span beam with different span lengths. Such beams are commonly used in structural engineering, for example, as bridge girders.

The design domain as shown in Fig. 9 is discretized with a 30×200 FE mesh, where the bottom row of elements has a fixed density of one. This guarantees that material is always

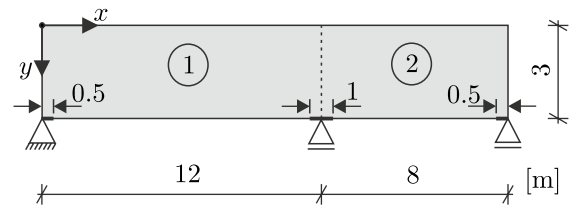
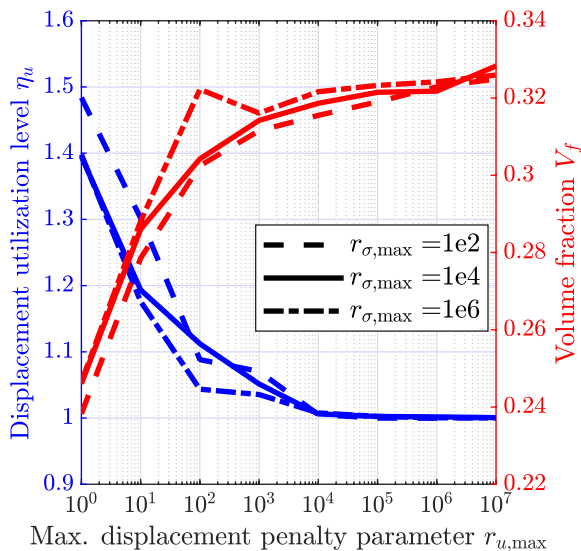
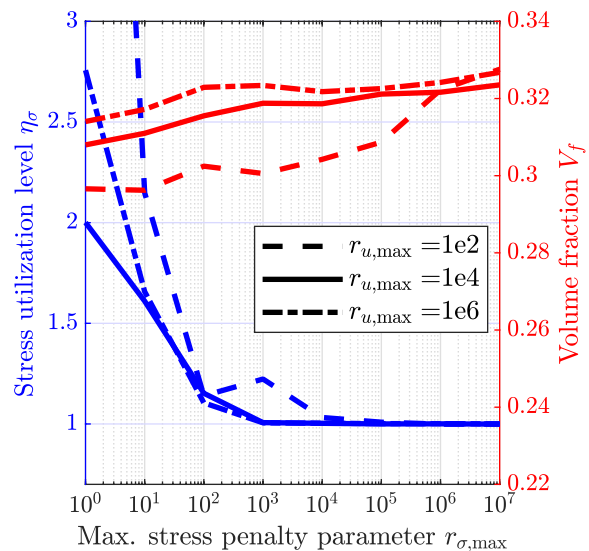


Fig. 9 Design domain and boundary conditions for the two-span beam example



(a) Displacement utilization level and volume fraction depending on $r_{u,max}$ for three different values of $r_{\sigma,max}$



(b) Stress utilization level and volume fraction depending on $r_{\sigma,max}$ for three different values of $r_{u,max}$

Fig. 8 L-shaped structure—study on the influence of the penalty parameters using stress and displacement constraints according to Table 3

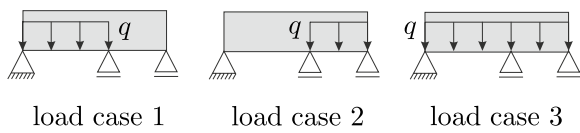


Fig. 10 Two-span beam—traffic load for the respective load case

Table 5 Parameter values used for the two-span beam in particular

Parameter	Symbol	Value	Unit
Young’s modulus	E_0	2.1 e8	kN/m ²
Poisson’s ratio	ν	0.3	–
Plate thickness	t	0.01	m
Traffic load	q	175	kN/m
Limit stress	σ_{lim}	2.35 e5	kN/m ²
Vertical disp limit left	$u_{y,lim}^{(1)}$	0.012	m
Vertical disp limit right	$u_{y,lim}^{(2)}$	0.008	m
Initial (uniform) phys. density	$\bar{\rho}_0$	0.5	–
Filter radius	R	0.2	m

accessible at the point of load application. The material properties are based on steel S235, as shown in Table 5.

Load cases: The two-span beam is subjected to a traffic load q , which is applied to the bottom-most row of nodes of the beam. This single load case is discussed in Sect. 4.2.1. In a real-world scenario, the traffic load may or may not be active. Therefore, $N_{lc} = 3$ different load cases are investigated, as depicted in Fig. 10. These load cases lead to the largest span moments and the largest support moment in a beam model of the problem. In none of these situations, the constraints may be violated. This example is discussed in Sect. 4.2.2. Further, the gravity load (self-weight) of the structure can be considered. This is discussed in Sect. 4.2.3, where the effect of the effective mass density γ_0 on the resulting topology is examined.

Stress constraints: In general, stress constraints should be imposed for every element in every load case. This leads to a total number of $N_e \cdot N_{lc} = 18,000$ stress constraints for this example. However, the elements near the support are excluded from the stress evaluation due to singularity effects. Precisely, the four bottom rows of elements are excluded from the stress constraint evaluation on a width of seven elements for the outer and 14 elements for the mid support. The density of these elements is fixed to one and they are plotted with a stress utilization level of zero in the plots below.

Displacement constraints: Of particular interest are the displacement constraints. In design codes, the admissible displacements are often specified as fraction of the respective span length L_i . In this case, a limit of $L_i/1000$ is set. Using local constraints, displacement limits are applied to



Fig. 11 Topology 1—optimum for the two-span beam subjected to load case 3 only

Table 6 Topology 1—utilization levels

Load case	η_σ	$\eta_u^{(1)}$	$\eta_u^{(2)}$
1	3.109	1.827	0.056
2	3.404	0.064	2.911
3	1.003	1.001	0.997



Fig. 12 Topology 2—optimum for the two-span beam considering load case 1, 2, and 3

the bottom row of nodes. Two different regions are distinguished: The left span ① with vertical displacement limit $u_{y,lim}^{(1)}$ and the right span ② with limit $u_{y,lim}^{(2)}$.

4.2.1 Single load case

For reference, the optimization is first performed using only load case 3, i.e., the traffic load is present on both spans. The resulting topology 1 is depicted in Fig. 11, while the corresponding utilization levels according to (50) and (51) are given in Table 6.

From Table 6, it can be seen that the optimizer does indeed generate a topology that meets the requirements for load case 3. However, applying load case 1 and 2 to the optimized structure, utilization levels greater than one are reached. This means that multiple load cases should be considered within the TO, where the traffic load may or may not be active.

4.2.2 Combination of three load cases

The optimal topology taking into account all three load cases is presented in Fig. 12. Compared to the topology of just using one load case, see Fig. 11, the required volume fraction is increasing from 0.380 to 0.453.

Concerning the stress distribution shown in Fig. 13, it can be seen that load case 1 and 2 generate high stresses in the center of the left and right span, respectively. The proximity of the mid support has a low utilization in those cases. For load case 3, the highest stress occurs at the mid support, while the stresses at the centers of the spans are slightly lower than those reached in case 1 or 2. Some elements are

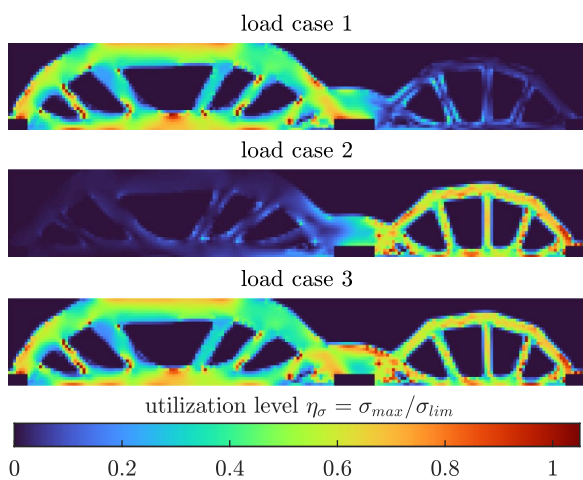


Fig. 13 Topology 2—stress utilization level for the respective load case

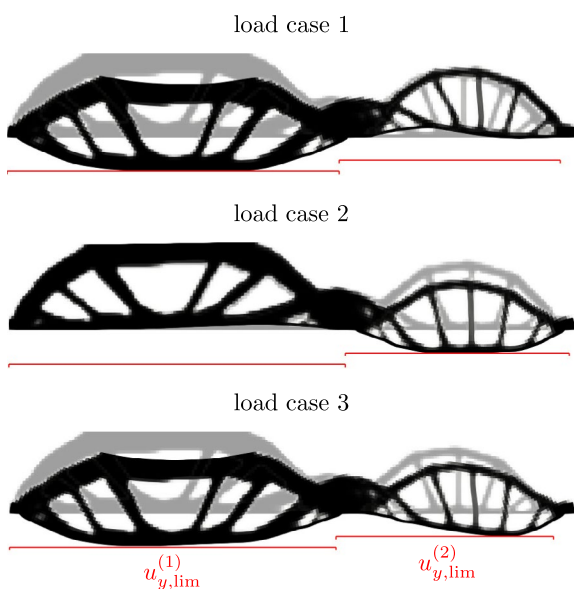


Fig. 14 Topology 2—displacement for the respective load case, scaling factor 100

Table 7 Topology 2—utilization levels

Load case	η_σ	$\eta_u^{(1)}$	$\eta_u^{(2)}$
1	1.002	1.000	0.042
2	0.990	0.000	1.000
3	1.003	0.970	1.000

stressed to the limit, but most of them have a lower stress than admissible. Overall, the material is not fully utilized in terms of stresses.

The displacements shown in Fig. 14 exactly reach their corresponding limit, see also Table 7. It is therefore

Table 8 Volume fraction for the two-span beam depending on the effective mass density

Effective mass density γ_0 [kN/m ³]	Volume fraction V_f [-]
0	0.385
10	0.386
100	0.388
1000	0.414
3000	0.475
5000	0.602

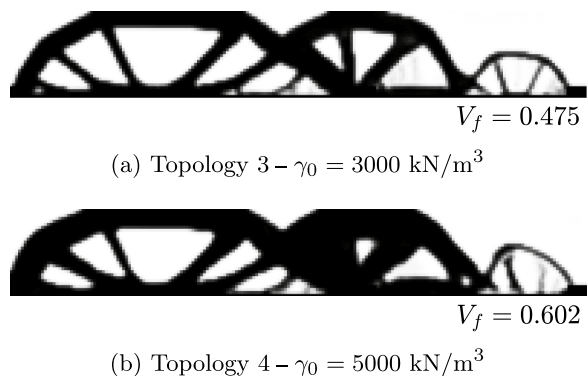


Fig. 15 Optimal topologies for the two-span beam subjected to load case 3 and gravity load, using different effective mass densities

concluded that both constraints are relevant in this problem, resembling the case presented in Fig. 5b.

4.2.3 Self-weight

Complementary, the influence of the self-weight is investigated. In order to avoid the parasitic effect, the RAMP approach is used instead of the SIMP approach, as implemented in Giraldo-Londoño and Paulino (2020). Only load case 3 is considered in this section. A study is conducted on how the resulting topology changes when varying the effective mass density γ_0 . The results are given in Table 8. It is observed that the volume fraction generally increases for higher values of γ_0 . However, for $\gamma_0 < 1000$ kN/m³, the volume fraction increases very slowly. It is inferred that the gravity load has only a minor influence in this range. As the parameters used for this example are based on steel S235, a realistic corresponding effective mass density is $\gamma_0 = 78.5$ kN/m³, in which case the self-weight is practically irrelevant. Nevertheless, the self-weight is highly relevant in other scenarios and its influence can be unknown beforehand. Further, the fact that self-weight is not an issue in this case highlights the efficiency of the optimized topology in terms of minimum material usage. It is also noted that for zero gravity load, the RAMP approach leads to

similar results compared to the SIMP approach, which is highlighted by comparing the resulting volume fraction $V_f = 0.385$ for $\gamma_0 = 0$ to $V_f = 0.380$ in Fig. 11. To illustrate the effect of a high effective mass density on the optimal topology, the optimization results for (a) $\gamma_0 = 3000 \text{ kN/m}^3$ and (b) $\gamma_0 = 3000 \text{ kN/m}^3$ are depicted in Fig. 15.

5 Conclusion

In this paper, a TO problem formulation is presented and solved that replicates common structural engineering problems as closely as possible. The volume of the structure is minimized with local stress and displacement constraints for varying load cases. The advantages of this formulation for practical applications are summarized as follows:

- Volume minimization instead of performance maximization is used, because the volume is usually unknown beforehand, but performance requirements are given.
- The optimization problem includes the common requirements strength and stiffness simultaneously.
- Stress constraints and displacement constraints represent practical requirements directly.
- Local constraints allow for different displacement limits in different structural regions.

The proposed optimization problem is solved by means of the AL method. The derivation of the gradient shows that an implementation of local displacement constraints based on the AL method is possible and can be combined with local stress constraints.

Moreover, the presented approach is highly modular because the AL method is based on a large sum of constraint terms. This means additional load cases or constraints for specific elements or nodes can easily be included by extending the sum of constraints. This allows one to adapt the presented TO approach to different structural engineering problems. Additionally, further investigations should be made in order to extend the optimization problem to include local buckling constraints.

Promising results are obtained for two examples. Based on the L-shape benchmark example, the method is compared with formulations using only a single type of constraints, while the two-span beam example shows the effect of applying multiple load cases. It is observed that for some cases, the combined stress- and displacement-constrained formulation yields different results compared to a solely stress- or displacement-constrained formulation, highlighting the necessity for the multiconstrained approach. Further, it is noted that a purely displacement-constrained approach leads to useful solutions only for very specific constrained regions. This can be the reason why this approach is unpopular

compared to approaches using the strain energy (compliance). However, simultaneous stress constraints open up the possibility to successfully apply a wider variety of displacement constraints and to generate structures where displacements are critical for one part, and stresses are critical for another part.

Nonetheless, the presented approach has some disadvantages. It involves a lot of numerical values such as the penalty parameters and number of iteration steps that need to be calibrated in order to get useful results. It is desirable to reduce the amount of parameters in order to get a more robust approach. In the author's opinion, a formulation purely based on Lagrange multipliers should be investigated, as it involves no penalty parameters.

Furthermore, it should be mentioned that the proposed optimization problem has local optima. The steepest descent method cannot account for this property. In fact, it cannot be guaranteed that the topologies presented in this paper represent the global optimum. This does not render the solution useless from engineering perspective, as long as the obtained volume fraction is at least close to the lowest feasible one. Nevertheless, the application of other optimization algorithms, see, e.g., Rojas-Labanda and Stolpe (2015) and Zhang and Norato (2018), should be investigated for the proposed problem.

Appendix A: Optimization algorithm

As optimization algorithm, the SDM formulation used in da Silva et al. (2021) is implemented. The full algorithm, which consists of the update scheme for the design variables after each iteration and the AL subproblem update, is repeated here for the sake of completeness.

Appendix A.1: SDM update scheme

The update scheme for the design variables is described in Appendix A of da Silva et al. (2021), while the original version is introduced in da Silva et al. (2017). The same settings for the step length and move limits are used.

1. *Sensitivity analysis*: Compute the gradient of the AL function $\mathbf{G} = \nabla_{\rho} L$ according to Sect. 3.2.
2. *Set move limits*: A lower move limit ρ_e^{inf} and upper move limit ρ_e^{sup} are calculated based on the two previous iterations as

$$d_e = (\rho_e^{(b)} - \rho_e^{(b-1)})(\rho_e^{(b-1)} - \rho_e^{(b-2)}), \quad (\text{A1})$$

$$\delta_e = \begin{cases} \max(0.7 \delta_e, 0.001) & d_e < 0 \\ \min(1.1 \delta_e, 0.1) & d_e > 0 \end{cases}, \quad (\text{A2})$$

$$\rho_e^{\text{inf}} = \rho_e^{(b)} - \delta_e, \tag{A3}$$

$$\rho_e^{\text{sup}} = \rho_e^{(b)} + \delta_e, \tag{A4}$$

where d_e and δ_e are auxiliary variables; $\delta_e = 0.1$ is used for the initial iterations.

3. Update the design variables:

- reset the gradient contributions at the bound constraints, as

$$G_e^{\text{new}} = \begin{cases} 0 & \text{if } \rho_e^{(b)} = 1 \text{ and } G_e < 0 \\ 0 & \text{if } \rho_e^{(b)} = 0 \text{ and } G_e > 0 \\ G_e & \text{otherwise} \end{cases}. \tag{A5}$$

- compute $\rho^{(b+1)}$ as

$$\rho_e^{(b+1)} = \max \left(\rho_{\min}, \max \left(\rho_e^{\text{inf}}, \min \left(\rho_e^{(b)} - \Psi \frac{G_e^{\text{new}}}{\|G_e^{\text{new}}\|_{\infty}}, \min(\rho_e^{\text{sup}}, 1) \right) \right) \right) \tag{A6}$$

using the unitary step length $\Psi = 1$.

Appendix A.2: Subproblem update scheme

The update scheme for each AL subproblem is based on the stress-constrained formulation presented in da Silva et al. (2021), applied also for the displacement constraints in this paper. After $N_{\text{it}}^{\text{sub}}$ iterations, the Lagrange multiplier estimates are updated according to (48) as follows:

$$\lambda_i^{(a+1)} = \max \left(0, \lambda_i^{(a)} + r_i^{(a)} g_i(\bar{\rho}) \right), \tag{A7}$$

where every entry λ_i of the stress or the displacement Lagrange multiplier estimate is zero, initially. This is repeated until the last subproblem is reached after $N_{\text{it}}^{\text{min}}$ iterations. The total number of iterations $N_{\text{it}}^{\text{tot}}$ is larger in order to reach full convergence for the last subproblem. In this paper, a fixed number $N_{\text{it}}^{\text{tot}}$ is used, but it is also possible to apply a convergence criterion to the last subproblem.

Further, the threshold projection parameter β and the penalty parameters r_i are updated as

$$r_i^{(a+1)} = \min \left(r_i^{(a)} \left(\frac{r_{i,\text{max}}}{r_{i,0}} \right)^{\frac{N_{\text{it}}^{\text{sub}}}{N_{\text{it}}^{\text{min}} - N_{\text{it}}^{\text{sub}}}}, \frac{r_{i,\text{max}}}{N_i} \right), \tag{A8}$$

$$\beta^{(a+1)} = \min \left(\beta^{(a)} \left(\frac{\beta_{\text{max}}}{\beta_0} \right)^{\frac{N_{\text{it}}^{\text{sub}}}{N_{\text{it}}^{\text{min}} - N_{\text{it}}^{\text{sub}}}}, \beta_{\text{max}} \right), \tag{A9}$$

such that they increase from β_0 to β_{max} and $\frac{r_{i,0}}{N_i}$ to $\frac{r_{i,\text{max}}}{N_i}$, respectively. Note that the penalty parameters are normalized by the corresponding number of constraints N_i . A stress penalty parameter r_{σ} and a displacement penalty parameter r_u are distinguished in this case.

Moreover, the minimum design density can be updated according to (23) as follows:

$$\rho_{\min}^{(a+1)} = \kappa + \frac{1}{\beta^{(a+1)}} \operatorname{atanh} \left(-\tanh(\beta^{(a+1)} \kappa) + \bar{\rho}_{\min} \left(\tanh(\beta^{(a+1)} \kappa) \tanh(\beta^{(a+1)} (1 - \kappa)) \right) \right). \tag{A10}$$

This approach ensures that the minimum physical density $\bar{\rho}_{\min}$ is constant during the optimization.

Funding Open Access funding enabled and organized by Projekt DEAL. No funding was received to assist with the preparation of this manuscript.

Declarations

Conflict of interest The authors have no relevant financial or non-financial interests to disclose.

Replication of Results All numerical results can be reproduced with the presented methods in Sects. 2 and 3. Data and materials are available upon request to the corresponding author.

Open Access This article is licensed under a Creative Commons Attribution 4.0 International License, which permits use, sharing, adaptation, distribution and reproduction in any medium or format, as long as you give appropriate credit to the original author(s) and the source, provide a link to the Creative Commons licence, and indicate if changes were made. The images or other third party material in this article are included in the article’s Creative Commons licence, unless indicated otherwise in a credit line to the material. If material is not included in the article’s Creative Commons licence and your intended use is not permitted by statutory regulation or exceeds the permitted use, you will need to obtain permission directly from the copyright holder. To view a copy of this licence, visit <http://creativecommons.org/licenses/by/4.0/>.

References

Amstutz S (2010) Connections between topological sensitivity analysis and material interpolation schemes in topology optimization. *Struct Multidisc Optim* 43(6):755–765. <https://doi.org/10.1007/s00158-010-0607-6>

Andreassen E, Clausen A, Schevenels M, Lazarov BS, Sigmund O (2011) Efficient topology optimization in MATLAB using 88 lines of code. *Struct Multidisc Optim* 43(1):1–16. <https://doi.org/10.1007/s00158-010-0594-7>

Bendsøe MP (1989) Optimal shape design as a material distribution problem. *Struct Optim* 1:193–202. <https://doi.org/10.1007/BF01650949>

Bendsøe MP, Kikuchi N (1988) Generating optimal topologies in structural design using a homogenization method. *Comput Methods*

- Appl Mech Eng 71:197–224. [https://doi.org/10.1016/0045-7825\(88\)90086-2](https://doi.org/10.1016/0045-7825(88)90086-2)
- Bendsøe MP, Sigmund O (2003) Topology optimization: theory, methods, and applications. Springer, Cham
- Birgin EG, Martínez JM (2014) Practical augmented Lagrangian methods for constrained optimization, vol 10. SIAM, Philadelphia
- Bourdin B (2001) Filters in topology optimization. Int J Numer Methods Eng 50(9):2143–2158. <https://doi.org/10.1007/s00158-009-0452-7>
- Bruggi M, Duysinx P (2012) Topology optimization for minimum weight with compliance and stress constraints. Struct Multidisc Optim 46(3):369–384. <https://doi.org/10.1007/s00158-012-0759-7>
- Bruyneel M, Duysinx P (2004) Note on topology optimization of continuum structures including self-weight. Struct Multidisc Optim 29(4):245–256. <https://doi.org/10.1007/s00158-004-0484-y>
- Chen Z, Long K, Wang X, Liu J, Saeed N (2020) A new geometrically nonlinear topology optimization formulation for controlling maximum displacement. Eng Optim 53(8):1283–1297. <https://doi.org/10.1080/0305215x.2020.1781106>
- Cheng G, Guo X (1997) ϵ -relaxed approach in structural topology optimization. Struct Optim 13:258–266. <https://doi.org/10.1007/BF01197454>
- Clausen Anders, Andreassen Erik (2017) On filter boundary conditions in topology optimization. Struct Multidisc Optim 56(5):1147–1155. <https://doi.org/10.1007/s00158-017-1709-1>
- da Silva GA, Cardoso EL (2017) Stress-based topology optimization of continuum structures under uncertainties. Comput Methods Appl Mech Eng 313:647–672
- da Silva GA, Beck AT, Cardoso EL (2017) Topology optimization of continuum structures with stress constraints and uncertainties in loading. Int J Numer Methods Eng 113(1):153–178. <https://doi.org/10.1002/nme.5607>
- da Silva GA, Beck AT, Sigmund O (2019) Stress-constrained topology optimization considering uniform manufacturing uncertainties. Comput Methods Appl Mech Eng 344:512–537. <https://doi.org/10.1016/j.cma.2018.10.020>
- da Silva GA, Aage N, Beck AT, Sigmund O (2021) Local versus global stress constraint strategies in topology optimization: a comparative study. Int J Numer Methods Eng 122(21):6003–6036. <https://doi.org/10.1002/nme.6781>
- Deqing Yang, Yunkang Sui, Zhengxing Liu, Huanchun Sun (2000) Topology optimization design of continuum structures under stress and displacement constraints. Appl Math Mech 21(1):19–26. <https://doi.org/10.1007/bf02458535>
- Duysinx P, Bendsøe MP (1998) Topology optimization of continuum structures with local stress constraints. Int J Numer Methods Eng 43(8):1453–1478. [https://doi.org/10.1002/\(SICI\)1097-0207\(19981230\)43:8<3C1453::AID-NME480%3E3.0.CO;2-2](https://doi.org/10.1002/(SICI)1097-0207(19981230)43:8<3C1453::AID-NME480%3E3.0.CO;2-2)
- Duysinx P, Sigmund O (1998) New developments in handling stress constraints in optimal material distribution. In: 7th AIAA/USAF/NASA/ISSMO symposium on multidisciplinary analysis and optimization. American Institute of Aeronautics and Astronautics. <https://doi.org/10.2514/6.1998-4906>
- Fancello EA, Pereira JT (2003) Structural topology optimization considering material failure. Latin Am J Solids Struct 1(1):3–24
- Freitag S, Peters S, Edler P, Meschke G (2022) Reliability-based optimization of structural topologies using artificial neural networks. Probab Eng Mech 70:103356. <https://doi.org/10.1016/j.probe.2022.103356>
- Giraldo-Londoño O, Paulino GH (2020) A unified approach for topology optimization with local stress constraints considering various failure criteria: von Mises, Drucker-Prager, Tresca, Mohr-Coulomb, Bresler-Pister and Willam-Warnke. Proc R Soc A Math Phys Eng Sci 476(2238):20190861. <https://doi.org/10.1098/rspa.2019.0861>
- Giraldo-Londoño O, Paulino GH (2021) PolyStress: a MATLAB implementation for local stress-constrained topology optimization using the augmented Lagrangian method. Struct Multidisc Optim 63(4):2065–2097. <https://doi.org/10.1007/s00158-020-02760-8>
- Huang X, Xie YM (2009) Evolutionary topology optimization of continuum structures with an additional displacement constraint. Struct Multidisc Optim 40(1–6):409–416. <https://doi.org/10.1007/s00158-009-0382-4>
- Jog CS, Haber RB (1996) Stability of finite element models for distributed-parameter optimization and topology design. Comput Methods Appl Mech Eng 130(3–4):203–226. [https://doi.org/10.1016/0045-7825\(95\)00928-0](https://doi.org/10.1016/0045-7825(95)00928-0)
- Le C, Norato J, Bruns T, Ha C, Tortorelli D (2009) Stress-based topology optimization for continua. Struct Multidisc Optim 41(4):605–620. <https://doi.org/10.1007/s00158-009-0440-y>
- Li Q, Steven GP, Xie YM (1999) On equivalence between stress criterion and stiffness criterion in evolutionary structural optimization. Struct Optim 18:67–73. <https://doi.org/10.1007/BF01210693>
- Mathworks. Matlab r2023b, (2023)
- Norato JA, Smith HA, Deaton JA, Kolonay RM (2022) A maximum-rectifier-function approach to stress-constrained topology optimization. Struct Multidisc Optim 65(10):286. <https://doi.org/10.1007/s00158-022-03357-z>
- París J, Navarrina F, Colominas I, Casteleiro M (2008) Topology optimization of continuum structures with local and global stress constraints. Struct Multidisc Optim 39(4):419–437
- París J, Navarrina F, Colominas I, Casteleiro M (2010) Block aggregation of stress constraints in topology optimization of structures. Adv Eng Softw 41(3):433–441. <https://doi.org/10.1016/j.advensoft.2009.03.006>
- Ramani A (2010) Multi-material topology optimization with strength constraints. Struct Multidisc Optim 43(5):597–615. <https://doi.org/10.1007/s00158-010-0581-z>
- Ringertz UT (1985) On topology optimization of trusses. Eng Optim 9(3):209–218. <https://doi.org/10.1080/03052158508902514>
- Rojas-Labanda S, Stolpe M (2015) Benchmarking optimization solvers for structural topology optimization. Struct Multidisc Optim 52(3):527–547. <https://doi.org/10.1007/s00158-015-1250-z>
- Sigmund O (2007) Morphology-based black and white filters for topology optimization. Struct Multidisc Optim 33(4–5):401–424. <https://doi.org/10.1007/s00158-006-0087-x>
- Stolpe M, Svanberg K (2001) An alternative interpolation scheme for minimum compliance topology optimization. Struct Multidisc Optim 22(2):116–124. <https://doi.org/10.1007/s001580100129>
- Svanberg K (1987) The method of moving asymptotes—a new method for structural optimization. Int J Numer Methods Eng 24(2):359–373. <https://doi.org/10.1002/nme.1620240207>
- Wang F, Lazarov BS, Sigmund O (2010) On projection methods, convergence and robust formulations in topology optimization. Struct Multidisc Optim 43(6):767–784. <https://doi.org/10.1007/s00158-010-0602-y>
- Wang L, Xia H, Zhang X, Lv Z (2019) Non-probabilistic reliability-based topology optimization of continuum structures considering local stiffness and strength failure. Comput Methods Appl Mech Eng 346:788–809. <https://doi.org/10.1016/j.cma.2018.09.021>
- Xia H, Wang L, Liu Y (2020) Uncertainty-oriented topology optimization of interval parametric structures with local stress and displacement reliability constraints. Comput Methods Appl Mech Eng 358:112644. <https://doi.org/10.1016/j.cma.2019.112644>
- Xu S, Cai Y, Cheng G (2009) Volume preserving nonlinear density filter based on heaviside functions. Struct Multidisc Optim 41(4):495–505. <https://doi.org/10.1007/s00158-009-0452-7>
- Yang R, Chen C (1996) Stress-based topology optimization. Struct Optim 12:98–105. <https://doi.org/10.1007/BF01196941>
- Yin L, Yang W (2001) Optimality criteria method for topology optimization under multiple constraints. Comput Struct 79(20–21):1839–1850. [https://doi.org/10.1016/S0045-7949\(01\)00126-2](https://doi.org/10.1016/S0045-7949(01)00126-2)

- Zhang S, Norato JA (2018) Finding better local optima in topology optimization via tunneling. In: Volume 2B: 44th Design automation conference. American Society of Mechanical Engineers. <https://doi.org/10.1115/detc2018-86116>
- Zhang S, Li H, Huang Y (2020) An improved multi-objective topology optimization model based on SIMP method for continuum structures including self-weight. *Struct Multidisc Optim* 63(1):211–230. <https://doi.org/10.1007/s00158-020-02685-2>
- Zhou M, Rozvany GIN (1991) The COC algorithm, part II: topological, geometrical and generalized shape optimization. *Comput Methods Appl Mech Eng* 89(1–3):309–336. [https://doi.org/10.1016/0045-7825\(91\)90046-9](https://doi.org/10.1016/0045-7825(91)90046-9)

Publisher's Note Springer Nature remains neutral with regard to jurisdictional claims in published maps and institutional affiliations.